Multiobjective Optimization and Enhanced Design of an Ω-Shaped Current Sensor for WBG Devices

Xia Du, *Student Member, IEEE*, Liyang Du, *Student Member, IEEE*, Yuxiang Chen, *Member, IEEE*, Andrea Stratta, and Homer Alan Mantooth, *Fellow, IEEE*

***Abstract*—The rapid evolution of wide bandgap devices has posed significant challenges in current sensor design concerning bandwidth, compact size, and intricate integrator design. This article presents a high-bandwidth Ω-shaped current sensor, consisting of an Ω-shaped copper tube, Rogowski coil and an external integrator, to achieve precise switching current measurement. The designed structure allows easy integration into various current paths. And a multiobjective optimization based on a genetic algorithm and a finite element method is developed for the comprehensive design of the Rogowski coil. Subsequently, three optimized solutions of coil geometry with bandwidth and sensitivity as optimization objectives are selected for comparison. Moreover, an external differential integrator and its associated design guide are introduced. Finally, comprehensive double pulse tests are performed under 800 V/70 A conditions. The test results of the three distinct coils validate the effectiveness of the proposed automated optimization methodology and external integrator design. The Ω-shaped current sensor consistently exhibits a faster response and maintains over 10 mV/A sensitivity compared with a 30-MHz commercial Rogowski coil.**

***Index Terms*—Current sensor design, Rogowski coil, switching current measurement, wide bandgap (WBG) devices.**

I. Introduction

POWER electronics have gained increasing significance across various applications, including motor drives, power supplies, renewable energy systems, aircraft and electric vehicles, owing to the ongoing trend towards electrification [1], [2], [3], [4], [5]. Consequently, the need for precise current measurements has escalated significantly within these systems for facilitating close-loop control mechanisms, over-current protection, and effective power management [6], [7], [8]. In addition, the rapid evolution of wide bandgap (WBG) devices has amplified the focus on switching current measurement for evaluating the switching characteristics of power semiconductor devices [9], [10]. In a landscape where electrical systems continually push the boundaries of efficiency, density and speed [11], [12], the demand for high-performance current sensing technologies has intensified. These technologies must possess the capability to accurately capture fast-changing electrical currents while also integrating seamlessly into existing systems [13], [14], [15], [16].

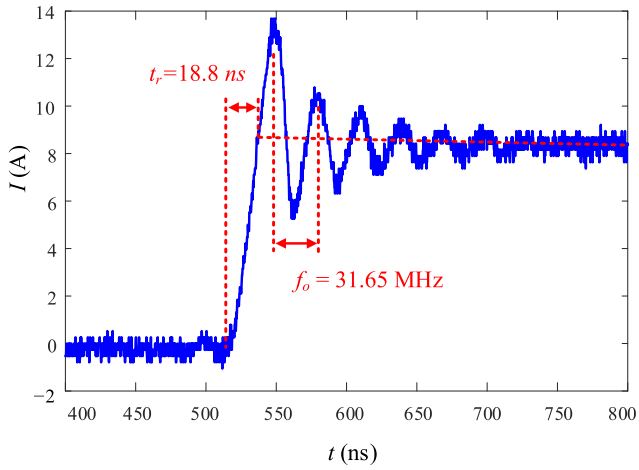

Fig. 1. Bandwidth requirement example of device SCT3120AL.

The bandwidth requirements of a current waveform in WBG power electronics applications are primarily determined by two factors: 1) switching transit time, which includes rising time t_r and falling time t_f of the current waveform during switching transients, and 2) oscillations or resonances that may occur in the current waveforms, caused by the output capacitance C_{oss} of devices under test (DUT) and power loop parasitic inductance L_{loop} [17]. To accurately capture the current information, the minimum required bandwidth of current sensors can be estimated according to (1) and (2) [18], [19], [20], [21], [22]. As a rule of thumb, it is recommended to have a bandwidth that is three to five times higher than the highest frequency in a current waveform to ensure sufficient accuracy and avoid signal distortion [22]. For example, considering the fast-switching speed SiC MOSFET SCT3120AL test waveform shown in Fig. 1, a current sensor with a bandwidth of 50 to 150 MHz is needed to capture the fast-rising time t_r 18.8 ns or a 31.65 MHz oscillation. Furthermore, as the research trends advance towards exploring ultra-wide-bandgap technologies, such as aluminum nitride, gallium oxide, and diamond, current sensors with even

Received 14 March 2024; revised 1 July 2024 and 17 October 2024; accepted 13 January 2025. Date of publication 23 January 2025; date of current version 26 February 2025. This work was supported by the NSF GRAPES Center under Grant 1939144. Recommended for publication by Associate Editor B. P. McGrath. *(Corresponding author: Xia Du.)*

Xia Du, Liyang Du, Yuxiang Chen, and Homer Alan Mantooth are with the Department of Electrical Engineering and Computer Science, University of Arkansas, Fayetteville, AR 72701 USA (e-mail: xiadu@uark.edu; liyangdu@uark.edu; yc041@uark.edu; mantooth@uark.edu).

Andrea Stratta was with the University of Arkansas, Fayetteville, AR 72701 USA. He is now with the Power Electronics Laboratory, University of California, Irvine, Irvine, CA 92697 USA (e-mail: astratta@uci.edu).

Color versions of one or more figures in this article are available at https://doi.org/10.1109/TPEL.2025.3533495.

Digital Object Identifier 10.1109/TPEL.2025.3533495

higher bandwidths, up to GHz, are required to meet the demands of these emerging applications

$$\mathrm{BW} = \frac{0.35}{\min(t_r, t_f)} \tag{1}$$

$$f_o = \frac{1}{2\pi\sqrt{C_{\mathrm{oss}} L_{\mathrm{loop}}}} \tag{2}$$

Currently, Rogowski coil based current sensors are drawing more attention due to their promising attributes, including potentially broad bandwidth, compact size because of an air core, various variants and ease of integration within different systems [23], [24], [25], [26], [27], [28], [29], [30], [31], [32], [33], [34], [35], [36], [37], [38], [39], [40], [41], [42], [43]. For higher bandwidth and better integration, Rogowski coil implementations have evolved from the traditional helical to different variants. One of the variants is the planar Rogowski coil, which can be configured in different shapes such as rectangular [23], [24], [25], [26], [27], [28], [29], [30], [31], [32], [33], toroidal [34], [35], [36]. They can be implemented either embedded in the power stages or standing alone as a discrete component. The Infinity-sensor is another variant of Rogowski coil, which are single-turn coils embedded in the power loop to be parallel with the current conductor [36], [37], [38], [39]. This configuration allows high bandwidth floating current sensing, with negligible insertion impedance and influence on switching performance. In addition, intended for high-temperature environment conditions, low temperature cofired ceramic-based current sensor is proposed to be integrated inside the power modules to realize higher integration level [40], [41]. Despite notable advancements, all the variants mentioned above are more suitable candidates for the applications that involve print circuit board (PCB)-based power stages. As an alternative method, the Ω-shaped current sensor has been reported in [42], [43], and [44] for laminated busbar-based power stages or highly integrated commutation cells. In [43], it is claimed that the Ω-shaped current sensor can achieve a bandwidth of up to 500 MHz with different configurations of the number of turns and integrator circuits. However, it lacks detailed guidance on coil construction and integrator design. In [44], it is a 5-turn copper wire wound on a plastic bobbin and inserted inside the Ω-shaped current path of a silicon carbide (SiC) power module. This design achieves an impressive bandwidth of 200 MHz and realizes seamless integration facilitated by advanced packaging technology. However, most of the research work focuses on module packaging optimization with the aim of achieving ultra-low inductance objective, thus it lacks detailed analysis of the coil design, and only a digital integration is applied in postprocessing procedures, which is not sufficient for real-time control and overcurrent protection. The absence of detailed information on both coil structure optimization and integrator design aspects remains a significant gap in the current research landscape for Ω-shaped current sensor.

Therefore, based on the preliminary study in [44], the main contribution of this article is that an optimization based on the design parameters of the coil structure towards the objectives of bandwidth and sensitivity is developed by combining MATLAB and ANSYS, which will give designers a comprehensive understanding of the coil design. To keep the integrity and provide a more comprehensive research and exploration on the development of the Rogowski coil based Ω-shaped current sensor, this article also explains all the critical design methods on the determination of the component values and the coordination of different stages of the external integrator design, thus paving the way for its continued utilization in cutting-edge technological advancements.

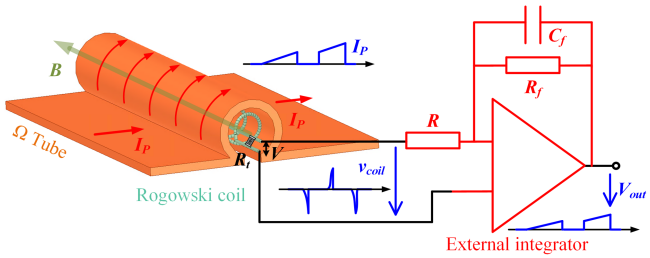

Fig. 2. Construction of the proposed current sensor.

The outline of this article is as follows. In Section II, the basic concept and modeling of the proposed Ω-shaped current sensor is introduced. Section III describes the multiobjective optimization of the coil structure towards an optimized tradeoff between bandwidth and sensitivity. In Section IV, the external integrator design process is demonstrated, and a differential topology is proposed to mitigate common mode noise. The entire design process is verified by double pulse test (DPT) experiments with the results provided in Section V. Finally, Section VI summarizes and concludes this article.

II. Modeling of the Ω-Shaped Current Sensor

A. Basic Concept

The proposed Ω-shaped current sensor consists of four key components: the primary current conductor termed the Ω tube, a secondary Rogowski coil, a terminal resistor R_t, and an external integrator, depicted in Fig. 2. The primary current conductor is a gapped copper tube. It is capable of being mounted over various current paths, including PCBs, busbars, or designated power modules. The secondary Rogowski coil, comprised of N turns of enameled wire wound around an air-core support structure, such as a 3-D-printed plastic or paper tube, resides within the Ω tube to detect magnetic field B variations. The terminal resistor serves the purpose of mitigating high-frequency resonance stemming from the parasitic elements inherent in the Rogowski coil. Finally, the external integrator is used to retrieve the information of the primary current I_P by integrating the output of Rogowski coil.

Based on Ampere's law (3), when an alternating current I_P passes through the Ω tube, a varying magnetic field B is generated, which will induce a voltage V at the terminal of the coil. According to Faraday's law (4), the induced voltage V is proportional to the changing rate of the primary current

$$\oint B\,(t)dl = \mu_0 N_p i\,(t) \tag{3}$$

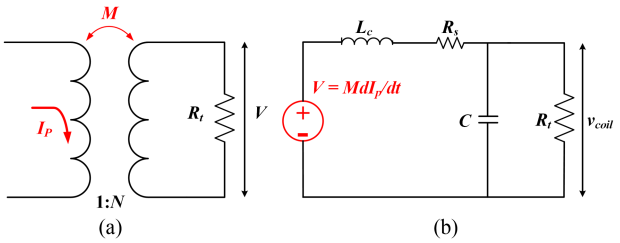

Fig. 3. Modeling of the proposed current sensor. (a) Ideal model. (b) Lumped stray parameter equivalent circuit.

$$V(t) = N\frac{d\Phi}{dt} = N \cdot \frac{d}{dt}\int B(t)dA = \frac{N \cdot A}{l}\mu_0\frac{di}{dt} \quad (4)$$

where N_p is the number of turns in the primary side, which is 1. N is the number of turns of the Rogowski coil, l is the length of the closed path that the magnetic field B passes through, and A is the cross-sectional area of coils. To simplify

$$V = M\frac{di}{dt} \quad (5)$$

where M is defined as the mutual inductance between the primary current conductor and the secondary Rogowski coil. Therefore, the output of the Rogowski coil is usually connected to an external electrical integrator circuit to integrate the induced voltage V, thus providing an output signal V_{out} that is proportional to the primary current I_P.

B. Modeling of the Proposed Ω-Shaped Current Sensor

Ideally, the induced electromagnetic voltage V will be directly fed to the integration stage to retrieve the I_P information as shown in Fig. 3(a). However, because of the parasitic elements in the Rogowski coil, the actual voltage v_{coil} sent to the integrator stage can be represented by a simplified, lumped parameter model as shown in Fig. 3(b). It consists of electromotive force V, self-inductance L_c of the secondary coil, series resistance R_s, parasitic capacitance C, and terminal resistor R_t. The transfer functions of terminal voltage v_{coil} over V and v_{coil} over I_P are shown in (6) and (7), respectively

$$A_v(s) = \frac{v_{\text{coil}}}{V} = \frac{1}{L_cCs^2 + (CR_s + L_c/R_t)s + (R_s + R_t)/R_t} \quad (6)$$

$$R_{\text{Rog}}(s) = \frac{v_{\text{coil}}}{I_P} = s \cdot M \cdot A_v(s) \quad (7)$$

To have a better understanding of how each parasitic element influences the bandwidth of the Ω-shaped current sensor, Bode plots with varied values of individual factors based on (6) are depicted in Fig. 4.

Referring to Fig. 4(a), an inadequate terminal resistor (R_t) imposes significant limitations on the bandwidth, while an overly large R_t induces resonant behavior. Consequently, the selection of R_t aims for a damping ratio (ζ) of 1 to achieve critical damping within the system. According to the standard form of Laplace-domain transfer function in a second-order dynamic

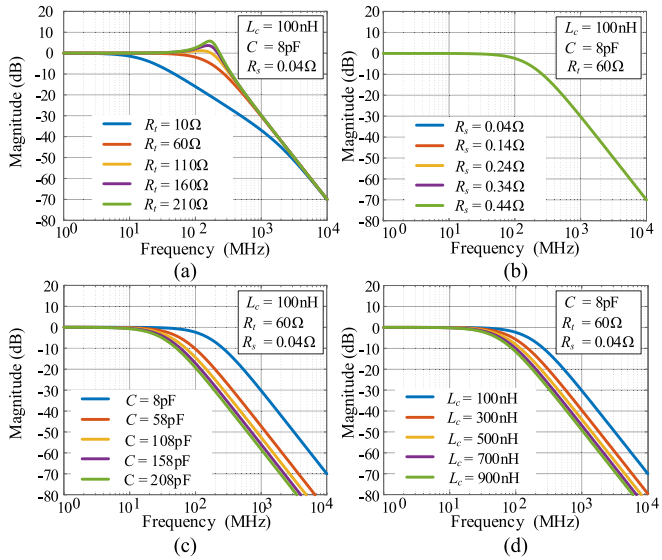

Fig. 4. Bode plots with different parasitic elements. (a) Terminal resistor R_t. (b) Parasitic resistor R_s. (c) Parasitic capacitor C. (d) Parasitic inductor L_c.

system, R_t can be calculated as follows:

$$R_t = \frac{L_c}{2 \cdot \sqrt{L_c \cdot C} - C \cdot R_s} \quad (8)$$

According to Fig. 4(b), the series resistance R_s demonstrates a negligible impact on the bandwidth. From the observations in Fig. 4(c) and (d), reducing parasitic capacitance C and parasitic inductance L_c, results in a larger bandwidth of the Rogowski coil. In addition, it is noteworthy that the parasitic capacitance C exerts a more dominant influence on the bandwidth compared to parasitic inductance L_c. Furthermore, concerning sensitivity, the Rogowski coil's sensitivity is primarily governed by the mutual inductance M according to (7). A larger mutual inductance M corresponds to a heightened signal-to-noise ratio (SNR) for the output voltage v_{coil}, thus, simplifying the integration stage design.

C. Design Challenges of the Rogowski Coil

The unique structure of the proposed Ω-shaped current sensor offers the advantages of easy integration and galvanic isolation. Subsequently, the remaining crucial objectives are bandwidth and sensitivity. According to Fig. 4, parasitic elements L_c and C dominate the bandwidth. The values of L_c, C are intricately tied to the physical structure of the proposed current sensor as depicted in Fig. 5, such as the dimension of the Ω tube (length M_L, height M_H, and depth M_D); Ω tube wall thickness d; slot L, which is the size of the gap on the Ω copper tube; number of turns (N) of the secondary winding; helix radius (R_{coil}), which is the size of the air-core supporter; pitch, which is the distance between two turns; and wire radius (R_{wire}), which is the thickness of the coil's conductor and isolation distance between coil and tube (D_{iso}). However, an explicit model for calculating parasitic parameters is lacking in existing literature. Consequently, accurately computing all parasitic elements during the design phase

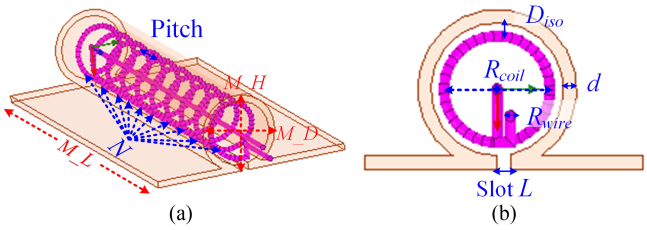

Fig. 5. Structure of Ω-shaped current sensor. (a) Side view. (b) Top view.

presents significant challenges. Furthermore, the sensitivity is also dependent on N, pitch and R_{coil} according to (5). Taking parameter N as an example, a higher N increases magnetic coupling, thus achieving higher sensitivity. However, increasing N also introduces higher parasitic inductance and capacitance, which in turn reduces the bandwidth. The existing literature falls short in providing a thorough analysis of how various design parameters collectively impact on the objectives. The challenge of designing an optimized structure to enhance both bandwidth and sensitivity arises from the nonmodeled behavior of parasitic parameters and the complexities of geometry. Therefore, there is a critical need for the development of a comprehensive methodology to optimize the performance based on the current sensor structure, thereby advancing current sensor design.

III. Multiobjective Design Optimization

For a comprehensive analysis of how the physical structure correlates with the performance of the Ω-shaped current sensor, analytical solutions for parasitic elements are not readily available due to the intricate structure. Therefore, using simulation to obtain parasitic parameters based on the real structure is a preferred approach. ANSYS Q3D, being a finite-element method software, is well-suited for simulating the physical structure and electromagnetic behavior of systems. Along with the compact size and ease of integration, bandwidth, and sensitivity serve as crucial performance metrics for current sensor optimization. In pursuit of an optimized structure that simultaneously enhances bandwidth and sensitivity, a multiobjective stochastic population-based optimization algorithm was employed for a comprehensive analysis of the Ω-shaped current sensor's design.

A. Design Specifications of the Simulation

Based on the structure shown in Fig. 5, there are seven design parameters that will affect the performance: Ω tube wall thickness d; slot L; number of turns (N); pitch; helix radius (R_{coil}); wire radius (R_{wire}); isolation distance (D_{iso}) and three dimension parameters: the maximum length of the current sensor M_L is defined as 50 mm and the maximum height/depth M_H/M_D is set to 10 mm considering size limitations in various applications. Given that this current sensor is specifically tailored for WBG devices, the number of turns is constrained to 30 to ensure a reasonably high bandwidth. Furthermore, it is imperative for pitch and R_{coil} to exceed 2 × R_{wire} to prevent any coil intersections between turns and enable the circular coil

TABLE I
Size Boundary of Design Variations

Variations	Minimum(mm)	Maximum(mm)
① Length of sensor M_L	/	50
② Height of sensor M_H	/	10
③ Depth of sensor M_D	/	②
④ Number of turns (N)	2	30
⑤ Wire radius (R_{wire})	0.05 (38 AWG)	0.25 (24 AWG)
⑥ Isolation distance (D_{iso})	0.2	1
⑦ Tube thickness (d)	0.5	3
⑧ Pitch	2.5 × ⑤	①/④
⑨ Helix radius (R_{coil})	2.5 × ⑤	②/2-⑥-⑦
⑩ Slot (L)	0.05	⑨

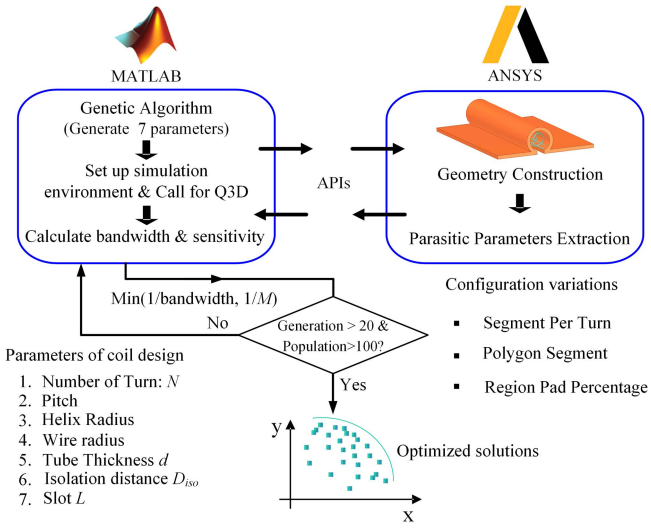

Fig. 6. Simulation procedure diagram.

shape, and they both are set at a minimum of 2.5 × R_{wire} to allow a safety margin. The comprehensive size boundary for all the design variables is detailed in Table I. Every constraint is established with reference to real-world applications and operational limitations inherent in the ANSYS software.

B. Optimal Automated Design Process

To facilitate automated optimization, MATLAB, embedded with Non-Dominated Sorting Genetic Algorithm II [45], [46], is integrated with ANSYS Q3D through Application Programming Interfaces as depicted in Fig. 6. The genetic algorithm is a method for solving optimization problems that is based on natural selection, a process that drives biological evolution. The genetic algorithm repeatedly modifies a population of individual solutions. At each step, the genetic algorithm selects individuals from the current population (to be parents) and uses them to produce individuals (to be children) for the next generation. Over successive generations, the population evolves toward an optimal solution. Therefore, a multiobjective stochastic population-based optimization algorithm, genetic algorithm, is developed in MATLAB to randomly generate a population of seven design parameters toward better performing of optimization objectives (bandwidth and sensitivity). Within the iterative process of a

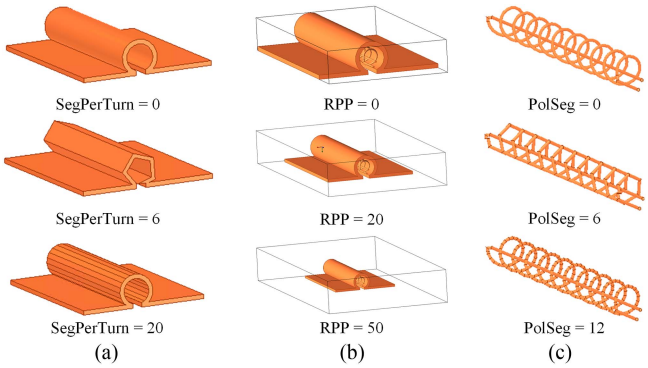

Fig. 7. Configuration variations of Ansys simulation. (a) Segment per turn. (b) Region pad percentage. (c) Polygon segment.

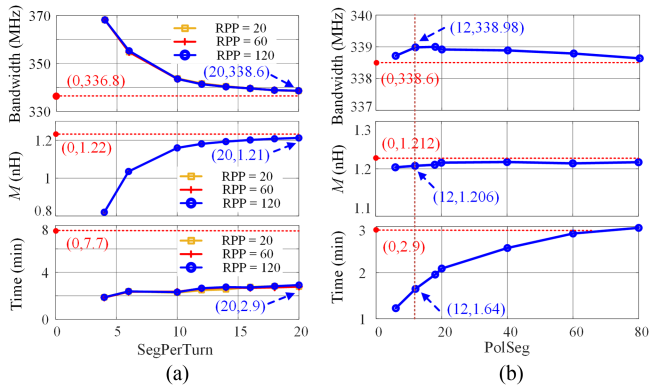

Fig. 8. Effect of configuration variations on cost. (a) Segment per turn, region pad percentage. (b) Polygon segment.

genetic algorithm, each set of populations forms a single generation. In this sequence, a new generation emerges based on the fitness evaluation of individuals selected stochastically from the current populations. Typically, the iteration terminates upon reaching either a predefined maximum number of generations or upon achieving a satisfactory fitness level aligned with the optimization objectives. Since the higher bandwidth, the higher mutual inductance, the better, the fitness function in (9) is applied to evaluate each population. And the iterative optimization terminates when it reaches the maximum generation. In this algorithm, the generation and population are defined as 20 and 100, respectively

$$\text{Min}\left(\frac{1}{\text{Bandwidth}}, \frac{1}{M}\right). \tag{9}$$

Based on each population, ANSYS Q3D will reconstruct the physical dimension of the Ω-shaped current sensor in each iteration. Subsequently, ANSYS extracts all the parasitic elements and mutual inductance, which are then transmitted to MATLAB for fitness evaluation for the next iteration process.

C. Minimization of the Computational Cost

For an automated design process, a good computational mesh is essential for achieving an accurate solution. Therefore, based on the structure of the current sensor, a maximum mesh size of 10, 4, and 0.2 are assigned to the region, Ω-shaped tube and coil, respectively, using the embedded adaptive iterative solver in ANSYS. Obtaining the optimal solution is undoubtedly vital, but it is equally crucial to consider the computational cost, such as simulation time. Striking a balance between accuracy and cost, three configuration variations in ANSYS are investigated as shown in Fig. 7. Fig. 7(a) segment per turn (SegPerTurn): the number of divisions or segments along the circumference or periphery of the Ω copper tube; Fig. 7(b) region pad percentage (RPP): it defines the size of the vacuum region for the simulation boundary; Fig. 7(c) polygon segment (PolSeg): the number of segments that approximate the contours of the windings. One principle that needs to be emphasized is that when setting SegPerTurn or PolSeg to 0, it signifies that there are no segments along the length of the tube or winding. In this configuration, the structure of the Ω-shaped current sensor is treated as a continuous surface without any discretization along its length, which has the highest accuracy in capturing the behavior of the physical system. Therefore, the performance in this configuration will be the benchmark for cost minimization.

The simulation results are depicted in Fig. 8. To control variables, polygon segment is set to be 0 initially, Segments per Turn and Region Pad Percentage are set to different values to investigate their impact on the accuracy indices (bandwidth, mutual inductance) and cost index (simulation time). Referring to Fig. 8(a), it is observed that the RPP does not significantly influence the accuracy indices, and the cost index simulation time is slightly less when RPP is set to 20. As for SegPerTurn, the simulation time stabilizes at approximately 3 min with its increasing. Moreover, it is worth noting that higher values of SegPerTurn contribute to increased accuracy compared to the benchmark, and when SegPerTurn = 20, the accuracy indices nearly approach the benchmark. Therefore, the RPP and SegPerTurn both are set up as 20 with 0.53% error for bandwidth and 0.82% error for mutual inductance to further investigate the effect of polygon segmentation.

The simulation results of various polygon segment values are shown in Fig. 8(b). It appears that changes in Polygon Segment do not significantly influence bandwidth and mutual inductance. However, it has a clear impact on simulation time. Striking a balance between accuracy and efficiency, the Polygon Segment is set to 12 to minimize simulation time to 1. 6 min per iteration while maintaining an error margin of 0.11% for bandwidth and 0.5% for mutual inductance.

D. Optimization Results

All the simulated scenarios (colored dots) are shown in Fig. 9. Each dot marker corresponds to a different combination of the seven geometry parameters. It is obvious that there is a compromise between bandwidth and sensitivity. The optimal design points (filled marker dots) form the Pareto-front of each generation are considered optimal solutions. During these optimal solutions, it is possible to maximize bandwidth at the expense

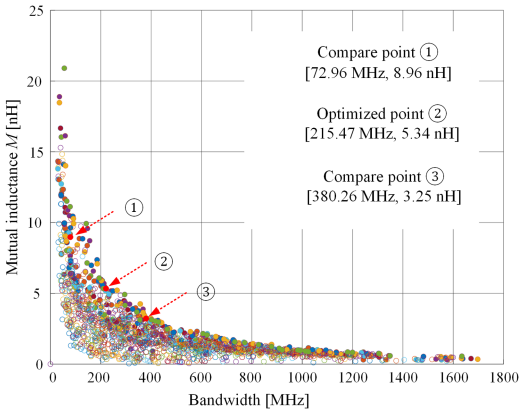

Fig. 9. Optimized simulation results.

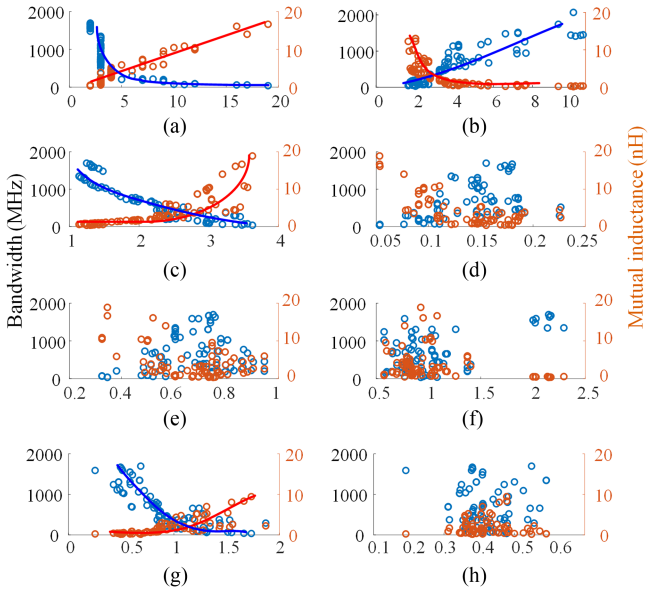

Fig. 10. Geometrical parameters' effects on objectives.

of sensitivity or vice versa, but they cannot both be improved at once. The selected optimization point ② is the one that offers a good compromise between bandwidth and sensitivity (Optimized point). To validate this simulation result, another two nonoptimization points (Compare point ① and Compare point ③) are selected to do the test comparison.

To gain a deeper insight into the impact of all seven design variables on the design objectives, Fig. 10 presents 2-D plots for each parameter in correlation with bandwidth and sensitivity based on all the optimized solutions from Pareto-front. Referring to Fig. 10(a), with the increasing of N, bandwidth is decreasing due to the introduced parasitic inductance and capacitance, and mutual inductance is increasing based on (4). The most significant trends are highlighted with a solid red line for mutual inductance and a solid blue line for bandwidth. Similarly, Pitch, and Helix radius R_{coil} also have a dominant effect on the performance indexes according to Fig. 10(b) and (c). Furthermore, according to Fig. 10(d)–(f), wire radius R_{wire},

TABLE II
DESIGN VARIABILITIES OF COMPARISON POINTS

Variations	Comparison Points		
	Compare point ③	Optimized point ②	Compare point ①
N	5	10	20
Pitch	6 mm	3 mm	1.5 mm
R_{coil}	2.7 mm	3.2 mm	2.5 mm
R_{wire}	0.15 mm	0.15 mm	0.14 mm
D_{iso}	0.55 mm	0.78 mm	0.67 mm
d	0.8 mm	0.8 mm	0.8 mm
Slot L	1 mm	1 mm	1 mm
Bandwidth	380.26 MHz	215.47 MHz	72.96 MHz
M	3.25 nH	5.34 nH	8.96 nH
L_c	48.91 nH	120.37 nH	461.58 nH
C	1.48 pf	1.87 pf	4.25 pf
L_Ω	2.97 nH		
3-D support	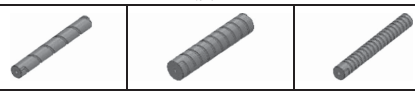		

isolation distance D_{iso}, and tube thickness d exhibit a broad distribution with different bandwidth and sensitivity M. This implies that these design variables do not have a significant effect on the design objectives. This can be understood as follows: tube thickness d primarily determines the current-carrying capability of the circuit, while R_{wire} and D_{iso} have minimal effects due to their limited size. For slot L, Fig. 10(g) seems to contradict theoretical analysis: larger L should result in weaker coupling, thereby reducing sensitivity, and lower parasitic capacitance, thereby increasing bandwidth. However, this discrepancy can be explained by the relatively minor effect of L on the objectives compared to the more dominant R_{coil}. Given that the boundary condition for slot L is: 0.05 mm $< L < R_{\text{coil}}$, L tends to be larger with larger R_{coil} during the optimization iteration according to Fig. 10(h), where L is clustered around 0.4–0.5 of R_{coil}, causing the impact of L exhibits similar trends as R_{coil}.

Design parameters and simulation results for the three selected points are shown in Table II. To simplify the current sensor design, the wire radius R_{wire} is set at 0.15 mm, the Ω-shaped conductor is made with 3.2 mm radius and 7 mm extension, the slot is set at 1 mm, and the tube thickness is set at 0.8 mm for all the three coils. According to the ANSYS simulation results, the Ω-shaped conductor introduces an insertion inductance of 2.97 nH to the main power loop, which can be minimized to 300 pH with further minimization or by directly integrated into the system without extension. To guarantee the coils are uniformly wound and centered within the Ω-shaped conductor, 3-D-printed plastic supports were designed with corresponding size and number of turns as the optimization results. For the slightly smaller Rogowski coil, layers of Kapton tape are applied on the bodies of the coils to ensure they are centered within the Ω-shaped tube.

IV. DESIGN AND COMPREHENSIVE GUIDE OF EXTERNAL INTEGRATOR

A. Integrator Topology Selection

There are three typical types of external integrator as shown in Fig. 11. Fig. 11(a) passive integrator, typically utilizing RC

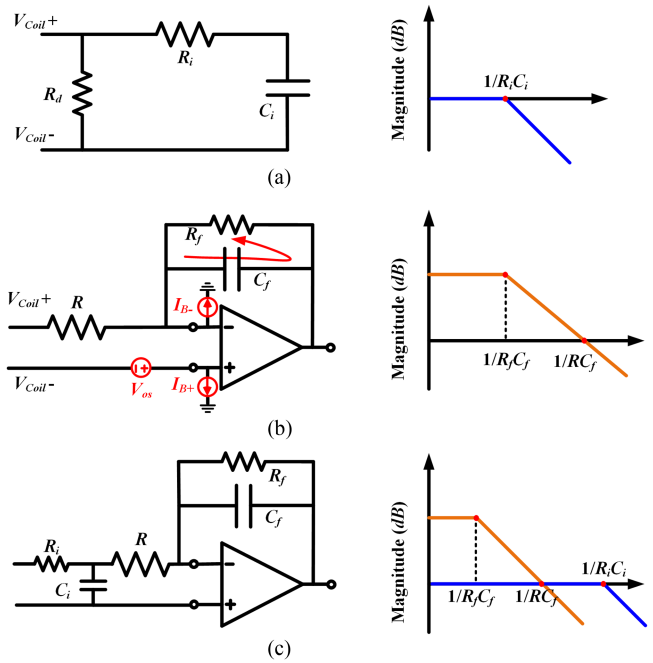

Fig. 11. Types of the external integrator. (a) Passive integrator with frequency response. (b) Active integrator with frequency response. (c) Combined integrator with frequency response.

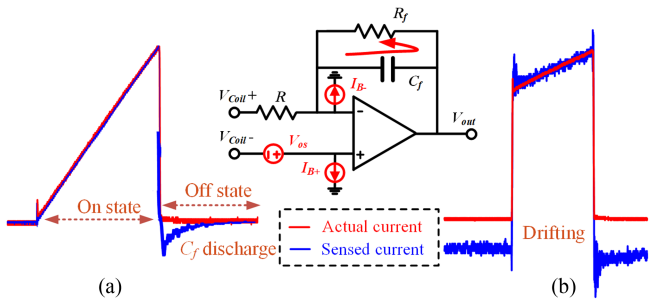

Fig. 12. Issues of the active integrator. (a) Discharge offset. (b) Drifting offset.

components; Fig. 11(b) active integrator, employing an operational amplifier to execute integration, and Fig. 11(c) combined integrator, normally comprised of an *RC* integrator followed by an active integrator. Normally, an inverting input for active integrator is preferred because the coil terminal voltage will transfer to the integrator output based on the noninverting integrator gain $1+R_f/R$.

Passive integrators are competitive because they only consist of passive components and do not require an external power source. However, their applications are limited as the corner frequency has to exceed 10 MHz to ensure proper integration while maintaining higher sensitivity (>10 mV).

Active integrators can offer a broader frequency response, improved noise performance and allow gain adjustment. However, there are some intrinsic errors for the active integrator. By taking pulse test as an example as shown in Fig. 12, first, during the off state, the feedback capacitor C_f begins to discharge its

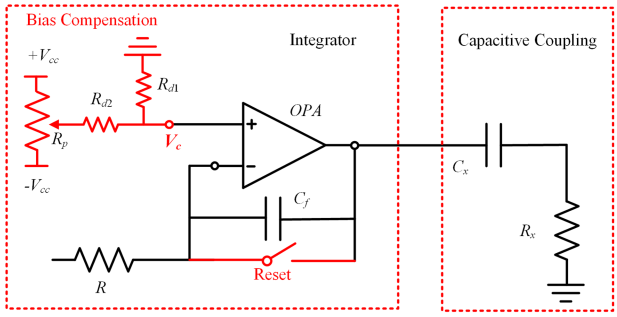

Fig. 13. Offset rejection of the active integrator.

stored energy through the resistor R_f, which will cause a negative output voltage decaying to zero as shown in Fig. 12(a). Second, the intrinsic input offset voltage V_{os} and input bias current I_B including I_{B+}, I_{B-} will cause output drift as shown in Fig. 12(b). Fortunately, all these issues can be mitigated through design.

The combined integrator offers a slightly broader bandwidth, but it requires intricate cutoff frequency and impedance matching to mitigate the fast drop gain distortion at high frequency [35]. Comparing these three types of integrators, the inverting active integrator is selected considering bandwidth, accuracy, and simplicity.

B. Offset Rejection Design

To address the R_f C_f feedback loop discharge offset in the conventional active integrator design, the feedback resistor is replaced by a reset switch as shown in Fig. 13 [47], [48]. When the power switch is ON, the reset switch will be OFF, thus the active integrator will be a pure integrator. When the power switch is OFF, the reset switch will be ON to short feedback capacitor C_f. Consequently, the output of the integrator will be reset to 0 at each switching cycle. As for the intrinsic input offset voltage and bias current of the Op-Amp, a bias compensation circuit is essential to cancel the drift at the initial condition. As depicted in Fig. 13, a potentiometer R_p is combined with resister R_{d1} and R_{d2} to provide the compensation voltage V_c. R_f will be relatively small at the initial condition because of the reset switch implementation and the effect of I_{B+} can be ignored in inverting configuration. Therefore, the total output error V_c caused by input offset voltage V_{os} and input bias current I_B will be $V_{os} \times (1+R_f/R) + I_{B-} \times R_f$. The compensation circuit is bipolar to guarantee error cancellation whether the polarity of the output error is positive or negative. Finally, to eliminate the residual offset, a capacitive coupling device (C_x R_x) is added between the integrator and the measurement stage.

C. Op-Amp, Resistor, and Capacitor Selection

To ensure a robust design for the external integrator, the process can be delineated into two key points: determination of component values and consideration of performance metrics.

To decide the value of the resistor and capacitor, the transfer function of the external integrator and Ω-shaped current sensor

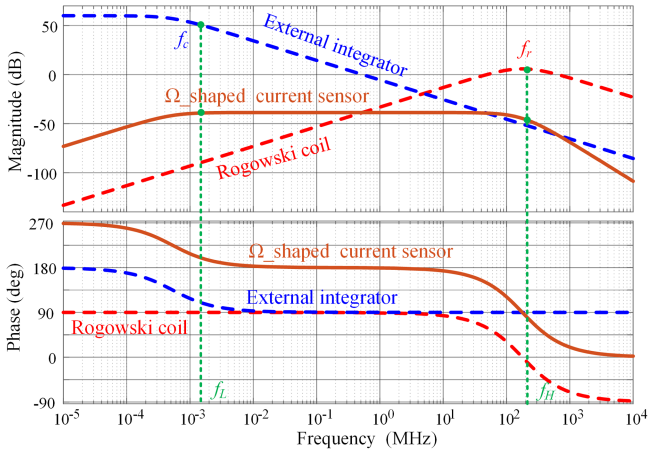

Fig. 14. Bode plot of Ω-shaped current sensor.

is denoted as (10) and (11)

$$H(s) = -\frac{R_f}{R} \cdot \frac{1}{C_f R_f s + 1} \tag{10}$$

$$R_\Omega(s) = R_{\text{Rog}}(s) \cdot H(s) \approx -\frac{M}{C_f \cdot R} \cdot A_v(s) \tag{11}$$

The gain, which is also called sensitivity, of the Ω-shaped current sensor is $|M/(C_f \times R)|$ based on (9). To guarantee the SNR large enough and the output voltage V_{out} within the op-amp power supply range V_{cc}, the C_f and R must satisfy the following equation:

$$S_{\min} \le \frac{M}{C_f \cdot R} \le S_{\max} \tag{12}$$

where $S_{\min}$ and $S_{\max}$ are the minimum and maximum sensitivity thresholds of the Ω-shaped current sensor that leads to an optimal measurement. In this design, $S_{\min}$ is set to 10 mV and $S_{\max} = V_{\text{cc}}/I_{\max}$, where $I_{\max}$ is the maximum current designed to be measured. In addition, to make sure the op-amp operates in normal condition, the resistor R has a minimum value to limit the maximum output current of the op-amp $i_{\text{opamp\_max}}$ as shown in the following equation according to [33]:

$$R \ge \left| \frac{v_{\text{coil\_max}}}{i_{\text{opamp\_max}}} \right| \tag{13}$$

where $v_{\text{coil\_max}}$ is the maximum coil terminal voltage. Considering the bandwidth of Ω-shaped current sensor, the Bode plot for the Rogowski coil, external integrator and Ω-shaped current sensor is shown in Fig. 14. It concludes that the lower bandwidth limit f_L is determined by the corner frequency f_c of the external integrator, and the higher bandwidth limit f_H is determined by the high bandwidth f_r of Rogowski coil. How to obtain a higher f_H has been well explained in Sections II and III, and the lower bandwidth f_L can be designed as follows:

$$f_L = \frac{1}{2\pi C_f \cdot R_f} \tag{14}$$

TABLE III
PARAMETERS OF THE EXTERNAL INTEGRATOR

Parameters	Value
R_t	90 Ω (③); 120Ω (②); 160 Ω (①)
$R_1/R_2/R_3/R_4$	100 Ω
R/C_f	R = 1 kΩ, C_f = 300 pF
Reset Switch	MAX4516
$R_{d1}/R_{d2}/R_p$	R_{d1} =2 kΩ, R_{d2} =1.02 kΩ, R_p =2 kΩ
R_c/C_c	R_c = 1 kΩ, C_c = 10 μF
R_x/C_x	R_x = 30 Ω, C_x = 100 pF
OPA1&OPA2	LTC6229
OPA3/OPA5	LTC6228
OPA4	OPA657

R_f is the impedance of the reset switch when the reset switch is OFF, which will be in MΩ. Therefore, to have a wide bandwidth for Ω-shaped current sensor, the value of C_f should be in pF to guarantee f_L to be in hundreds Hz.

Considering the performance of resistor and capacitor in high frequency, capacitors exhibiting lower Equivalent Series Resistance and Equivalent Series Inductance tend to perform more effectively by attenuating waveform ripples. When choosing resistors, opting for radio frequency resistors is advantageous for optimal performance. Certainly, when selecting an Op-Amp, crucial parameters to consider include gain bandwidth, slew rate, input bias current, input offset voltage, and input voltage noise. The gain bandwidth ideally should be three to five times greater than the current sensor bandwidth, which would be better insurance that the expected performance is achieved. Slew rate ought to exceed the measured current's slew rate. Input bias current, input offset voltage, and input voltage noise significantly influence measurement accuracy, hence, minimizing these values enhances integrator output precision. Furthermore, voltage feedback and unit-gain stable op-amps are preferred since they will be unconditionally stable at any gain, which relieves the designer of the burden of compensating circuits for stable operation.

D. External Integrator Scheme

The topology of the external integrator is shown in Fig. 15. First, to limit the impedance mismatch interference, a voltage follower is applied at each coil terminal to keep the $V_{\text{coil}}{}^+$, $V_{\text{coil}}{}^-$ fidelity. Then a differential topology is implemented to reduce the influence of the common-mode noise on the output as follows:

$$V_{d\_\text{out}} = V_C{}^+ \cdot \frac{1 + R_4/R_3}{1 + R_1/R_2} - \frac{R_4}{R_3} V_C{}^- \tag{15}$$

When $R_1 = R_2 = R_3 = R_4$, $V_{d\_\text{out}} = V_C{}^+ - V_C{}^-$, which will cancel the common-mode noise effectively. The clean signal laid a solid ground for the following integrator stage and capacitive coupling stage, which has been analyzed in Section IV-B. Finally, another follower is implemented between the capacitive coupling stage and the low pass filter RC stage to eliminate loading effects for filtering. All the components of the external integrator are listed in Table III.

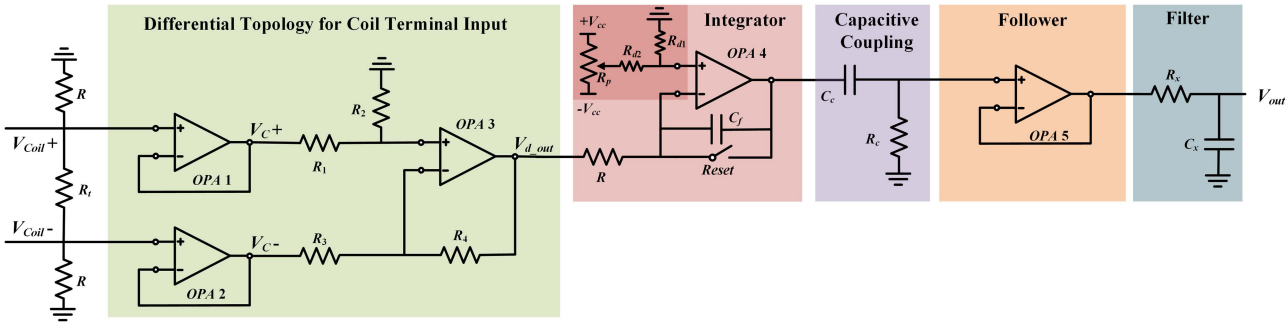

Fig. 15. Topology of external integrator.

TABLE IV
CONSTRUCTION OF THE Ω-SHAPED CURRENT SENSOR

Parts	Prototype
Primary Ω-shaped conductor	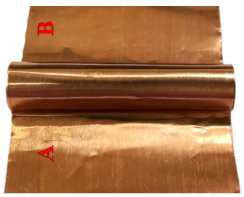
Secondary Rogowski coil	
External integrator	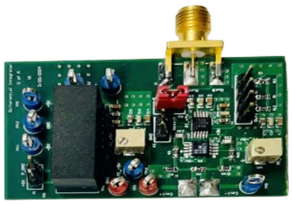

V. EXPERIMENTAL VALIDATION

A. Construction of Ω-Shaped Current Sensor

The construction of the Ω-shaped current sensor is detailed in Table IV. The primary Ω-shaped conductor is constructed by soldering two copper sheets (A and B) to the sides of a slotted brass cylinder. These copper extensions allow for easy installation onto the power board using screws. This configuration was designed for preliminary experimental validation. In practical applications, the Ω-shaped conductor will be directly integrated into the dedicated footprint along the current path, which can be located on a PCB board or busbar to ensure a strong connection and minimize insertion inductance. The secondary Rogowski coil is assembled using 0.15 mm enameled wire, wound around a 3-D-printed plastic support. The 3-D-printed supports were designed to ensure the coils are uniformly wound and centered within the Ω-shaped conductor. In addition, a wire-size through-hole is designed along the central axis of the support, allowing the coil to return the lead from one end through the center of the coil to the other end. This cancels the undesirable perpendicular magnetic noises. Then the two coil terminals are soldered to the external integrator board to retrieve the current information.

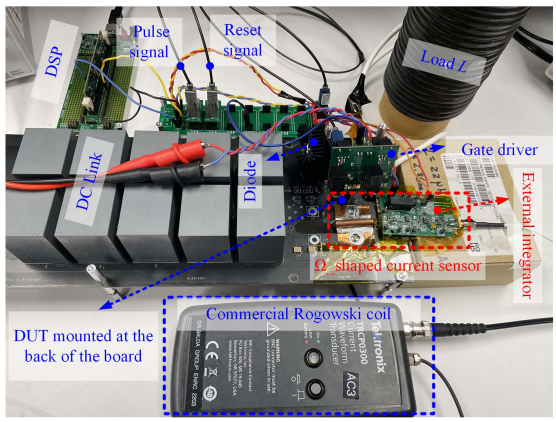

Fig. 16. Experimental setup.

B. Experimental Platform

A DPT setup was built to validate the Rogowski coil and external integrator design as shown in Fig. 16. The pulse waveform is generated by DSP TMS320F28335. The DUT is a 1.2 kV/63 A SiC MOSFET (C2M0025120D) from CREE. The upper freewheeling diode is a 1.2 kV/54 A SiC Schottky diode (C4D40120D). The isolated gate driver is designed with the recommended gate drive voltage of 20/−5 V and an external gate resistance of 5 Ω. The proposed Ω-shaped current sensor is placed between the DUT and the negative terminal of the dc link. The 30 MHz commercial Rogowski coil Tektronix TRCP0300 is placed on the drain leg of DUT. Three distinct Rogowski coils chosen from the optimization results were subjected to testing to verify the optimization process.

C. Experimental Results

The experiment was carried out at 800 V/70 A. Three Rogowski coils (compare point ①, optimized point ②, compare

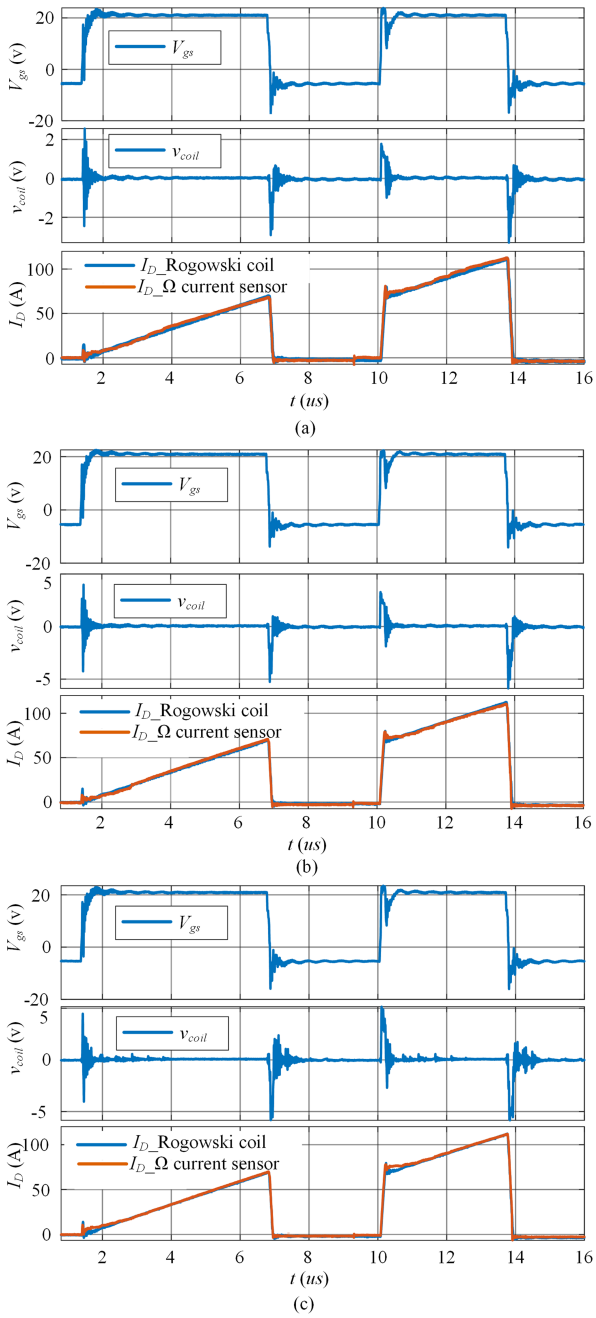

Fig. 17. DPT results with different number of turns (N) of Rogowski coil. (a) Coil ③. (b) Coil ②. (c) Coil ①.

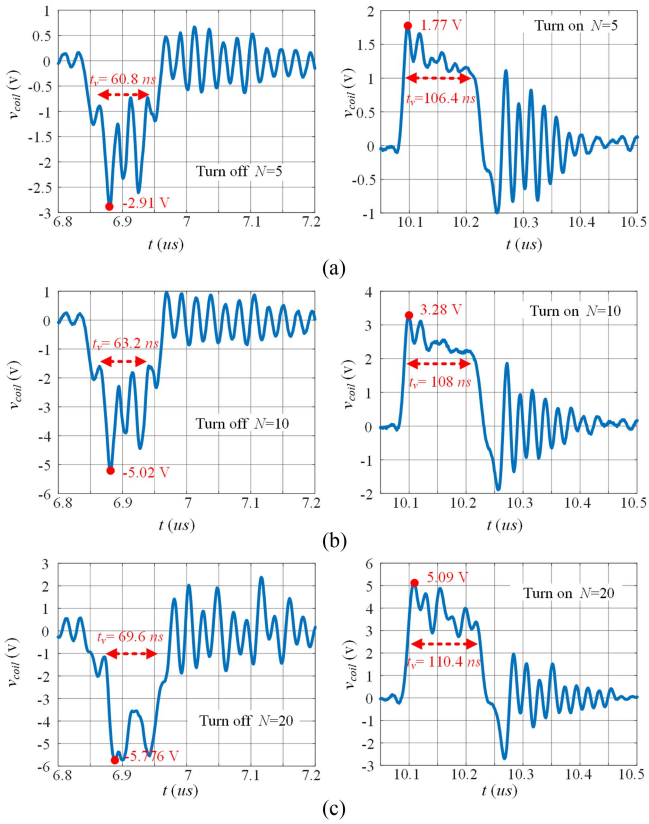

Fig. 18. Coil terminal voltage of switching transient. (a) Coil ③. (b) Coil ②. (c) Coil ①.

point ③) as mentioned in Table II are tested with the same external integrator except the terminal resistors R_t. The outcomes of these tests are illustrated in Fig. 17. Referring Fig. 17(a)–(c), the consistency between the measured drain current I_D obtained from commercial Rogowski coil and Ω-shaped current sensor validated the designs of both the Rogowski coil and external integrator.

The coil terminal voltage v_{coil} during the switching transient is shown in Fig. 18. According to $v_{\text{coil}} = M di/dt$, where M is in nH, the time duration t_v can interpret the switching speed of the primary current I_P when v_{coil} has a large and stable output. As listed in Table IV, it is 69.6, 63.2, and 60.8 ns during switching OFF transient, and 110.4, 108, and 106.4 ns during switching ON transient for coil ①②③ respectively. It concludes that the bandwidth of coil ③ > coil ② > coil ①, which matches with the optimization results. Furthermore, v_{coil} is 5.09, 3.28, and 1.77 V when DUT is turning ON, and 5.776, 5.02, and 2.91 V when DUT is turning OFF for coil ①②③. It concludes that the coil terminal voltage v_{coil} exhibits an increase corresponding to the larger sensitivity, aligning well with both simulation data of mutual inductance M and theoretical analysis $v_{\text{coil}} = M di/dt$. These comprehensive test outcomes serve as a robust validation of the optimization process.

The switching transient details of drain current I_D associated with the three distinct coils are visually presented in Fig. 19. The specifics of the test outcomes are detailed in Table V. The switching speed di/dt is computed based on the rate of change of the drain current (I_D) from 10% to 90%. Specifically, for the commercial Rogowski coil, the di/dt is 0.565 A/ns during the turn-ON transient and 0.696 A/ns during the turn-OFF transient. The conclusion drawn is that all current measurements of Ω-shaped current sensor are faster than the 30 MHz commercial Rogowski coil, and a smaller number of turns (N) corresponds to a faster sensing capability of the sensor. The tens of nanosecond fast transient retrieval further confirm the effectiveness of the external integrator's design. Furthermore, the mutual inductance M is calculated by the average of the mutual inductance during both turn-ON and turn-OFF transient, derived from the test results of v_{coil} and di/dt. The error

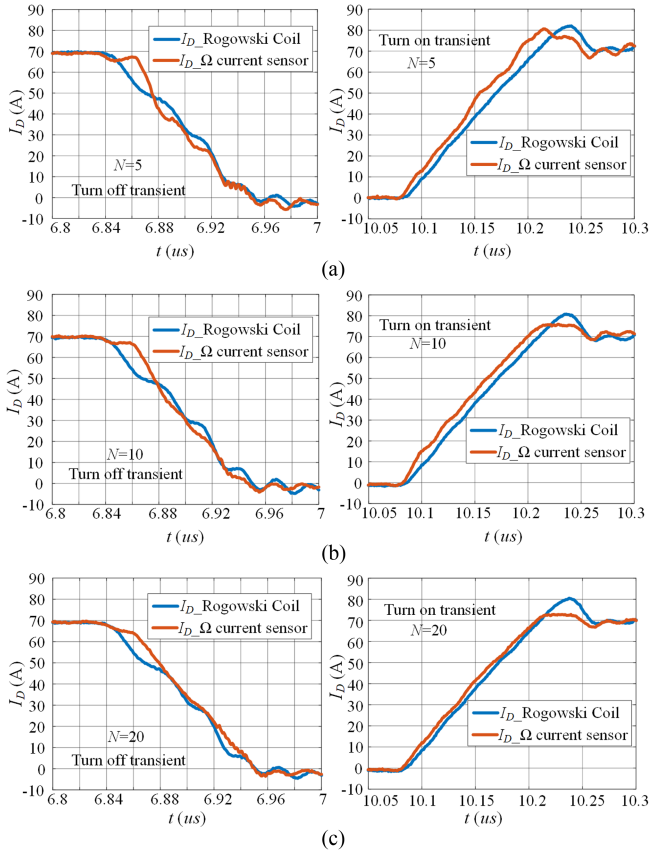

Fig. 19. Drain current switching transient. (a) Coil ③. (b) Coil ②. (c) Coil ①.

TABLE V
SWITCHING TRANSIENT DETAILS OF DPT

Parameters \ Coils		Coil ①	Coil ②	Coil ③
Number of turns N		20	10	5
Turn OFF transient	v_{coil} (V)	5.776	5.02	2.91
	t_v (ns)	69.6	63.2	60.8
	di/dt (A/ns)	0.710	0.873	0.893
Turn ON transient	v_{coil} (V)	5.09	3.28	1.77
	t_v (ns)	110.4	108	106.4
	di/dt (A/ns)	0.568	0.583	0.593
M (nH)		8.55	5.69	3.12
Sensitivity (mV/A)		27.5	18.7	12.1

between the calculated M and the simulated value outlined in Table II, are considered negligible. Finally, the sensitivity values for these three Rogowski coil designs are recorded at 27.5, 18.7, and 12.1 mV/A, respectively. Combining all the information from the DPT test, the consistent alignment observed between simulation and experimental outcomes robustly substantiates the integrity and accuracy of the entire design process.

D. Bandwidth Validation

To validate the bandwidth of the Ω-shaped current sensor, the step response of the current sensor with coil ① was investigated.

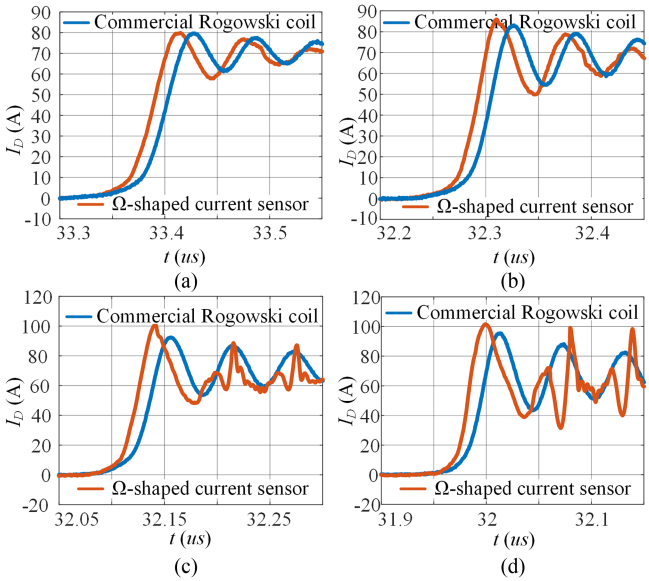

Fig. 20. Step response of the Ω-shaped current sensor. (a) $R_{\rm gate} = 5\ \Omega$. (b) $R_{\rm gate} = 2.5\ \Omega$. (c) $R_{\rm gate} = 1\ \Omega$. (d) $R_{\rm gate} = 0.5\ \Omega$.

TABLE VI
SWITCHING TRANSIENT DETAILS WITH DIFFERENT GATE RESISTOR CONFIGURATION

R_{gate}	Ω-shaped current sensor		Commercial Rogowski coil	
	t_r (ns)	di/dt (A/ns)	t_r (ns)	di/dt (A/ns)
5 Ω	36.2	1.55	38.8	1.44
2.5 Ω	29.4	1.91	34.5	1.63
1 Ω	23.6	2.36	31.4	1.78
0.5 Ω	19.2	2.92	25	2.25

To generate a current step, the upper switch of the DPT is configured as DUT, and the Ω-shaped current sensor is connected in series with the lower switch diode to sense the diode current. By decreasing the value of the gate resistor $R_{\rm gate}$, a faster current step I_D is generated.

Referring to Fig. 20, with the gate driver resistor varying from 5 to 0.5 Ω, the switching speed changes from 1.5 to approximately 3 A/ns. The Ω-shaped current sensor was able to track the switching transient and consistently responded faster compared to the 30 MHz commercial Rogowski coil. It is worthy to note that with the increasing switching speed, the Ω-shaped current sensor demonstrated higher peaks and higher frequency components, as shown in Fig. 20(c) and (d), indicating a higher bandwidth. The details of the switching transient are summarized in Table VI. The fastest rising time observed was 19.2 ns. To capture this fast-switching transient, the current sensor needs a bandwidth of (3–5) × (1), which is 55 to 91 MHz. Therefore, the Ω-shaped current sensor with coil ① has a bandwidth of at least 50 MHz, which aligns well with the optimization results in ANSYS.

VI. Conclusion and Discussion

This article introduced an integration-friendly Ω-shaped current sensor that can measure switching current of the WBG devices. The Ω-shaped current sensor design mainly includes two facets: Rogowski coil design and external integrator design. Addressing a research gap, the Rogowski coil's multiobjective optimization, achieved through a genetic algorithm, reconciles the compromise between bandwidth and sensitivity effectively. The proposed differential topology integrator design mitigates the common mode noise effectively and the comprehensive integrator design process provides a robust foundation for future research endeavors. The entire design process is validated under 800 V/70 A DPT. By comparing the test results of three distinct Rogowski coil designs, the optimization process was validated, and by comparing the drain current measurement obtained by Ω-shaped current sensor and 30 MHz commercial Rogowski coil, the integrity of the external integrator and the entire sensor design was proven. The proposed Ω-shaped current sensor delivers a bandwidth of at least 50 MHz and achieves over 10 mV/A sensitivity. The compact size and excellent performance in switching current measurements make it a promising candidate for integration within power modules, aligning with the trajectory of future advanced packaging technology and current sensor research.

References

[1] J. Lu, L. Zhu, G. Liu, and H. Bai, "Device and system-level transient analysis in a modular designed sub-MW EV fast charging station using hybrid GaN HEMTs + Si MOSFETs," *IEEE J. Emerg. Sel. Topics Power Electron.*, vol. 7, no. 1, pp. 143–156, Mar. 2019.

[2] J. Zeng, X. Du, and Z. Yang, "A multiport bidirectional DC–DC converter for hybrid renewable energy system integration," *IEEE Trans. Power Electron.*, vol. 36, no. 11, pp. 12281–12291, Nov. 2021.

[3] S. Gupta and S. K. Mazumder, "A differential-mode isolated AC/AC converter," *IEEE Trans. Power Electron.*, vol. 38, no. 10, pp. 12846–12858, Oct. 2023.

[4] X. Zhao, R. Phukan, C.-W. Chang, R. Burgos, D. Dong, and P. Asfaux, "Design and optimization of 2×211-kW SiC-based aircraft propulsion inverter system with high power density and high efficiency," in *Proc. IEEE Appl. Power Electron. Conf. Expo.*, 2023, pp. 1009–1016.

[5] R. Phukan et al., "Characterization and mitigation of conducted emissions in a SiC based three-level T-type motor drive for aircraft propulsion," *IEEE Trans. Ind. Appl.*, vol. 59, no. 3, pp. 3400–3412, May/Jun. 2023.

[6] A. E. Awwad and S. Dieckerhoff, "Short-circuit evaluation and overcurrent protection for SiC power MOSFETs," in *Proc. 17th Eur. Conf. Power Electron. Appl.*, 2015, pp. 1–9.

[7] L. Du et al., "Digital close-loop active gate driver for static and dynamic current sharing of paralleled SiC MOSFETs," *IEEE J. Emerg. Sel. Topics Power Electron.*, vol. 12, no. 2, pp. 1372–1384, Apr. 2024.

[8] J. Zeng, J. Ning, X. Du, T. Kim, Z. Yang, and V. Winstead, "A four-port DC–DC converter for a standalone wind and solar energy system," *IEEE Trans. Ind. Appl.*, vol. 56, no. 1, pp. 446–454, Jan./Feb. 2020.

[9] H. Li, S. Beczkowski, S. Munk-Nielsen, K. Lu, and Q. Wu, "Current measurement method for characterization of fast switching power semiconductors with silicon steel current transformer," in *Proc. IEEE Appl. Power Electron. Conf. Expo.*, 2015, pp. 2527–2531.

[10] Z. Zeng, J. Wang, L. Wang, Y. Yu, and K. Ou, "Inaccurate switching loss measurement of SiC MOSFET caused by probes: Modelization, characterization, and validation," *IEEE Trans. Instrum. Meas.*, vol. 70, 2021, Art. no. 1002014.

[11] H. A. Mantooth, M. D. Glover, and P. Shepherd, "Wide bandgap technologies and their implications on miniaturizing power electronic systems," *IEEE Trans. Emerg. Sel. Power Electron.*, vol. 2, no. 3, pp. 374–385, Sep. 2014.

[12] A. Bindra, "Wide-bandgap-based power devices: Reshaping the power electronics landscape," *IEEE Power Electron. Mag.*, vol. 2, no. 1, pp. 42–47, Mar. 2015.

[13] L. Shillaber, L. Ran, Y. Shen, and T. Long, "Gigahertz current measurement for wide band-gap devices," in *Proc. IEEE Energy Convers. Congr. Expo.*, 2020, pp. 2357–2363.

[14] D. Ying and D. A. Hall, "Current sensing front ends: A review and design guidance," *IEEE Sensors J.*, vol. 21, no. 20, pp. 22329–22346, Oct. 2021.

[15] B. Setera and A. Christou, "Challenges of overcoming defects in wide bandgap semiconductor power electronics," *Electronics*, vol. 11, no. 1, 2022, Art. no. 10.

[16] Z. Xin, H. Li, Q. Liu, and P. C. Loh, "A review of megahertz current sensors for megahertz power converters," *IEEE Trans. Power Electron.*, vol. 37, no. 6, pp. 6720–6738, Jun. 2022.

[17] "Understanding bandwidth requirement when measuring switching characteristics in power electronic applications," May 2021. [Online]. Available: https://www.keysight.com/us/en/assets/7122-1080/article-reprints/Understanding-bandwidth-requirements.pdf

[18] J. B. Witcher, "Methodology for switching characterization of power devices and modules," M.S. thesis, Dept. Elect. Eng, Virginia Polytech. Inst. State Univ., Blacksburg, VA, USA, 2003.

[19] C. Zhen, "Characterization and modeling of high-switching-speed behavior of SiC active devices," M.S. thesis, Dept. Elect. Eng., Virginia Polytech. Inst. State Univ., Blacksburg, VA, USA, 2009.

[20] Z. Zhang, B. Guo, F. F. Wang, E. A. Jones, L. M. Tolbert, and B. J. Blalock, "Methodology for wide band-gap device dynamic characterization," *IEEE Trans. Power Electron.*, vol. 32, no. 12, pp. 9307–9318, Dec. 2017.

[21] J. Chen, X. Du, Q. Luo, X. Zhang, P. Sun, and L. Zhou, "A review of switching oscillations of wide bandgap semiconductor devices," *IEEE Trans. Power Electron.*, vol. 35, no. 12, pp. 13182–13199, Dec. 2020.

[22] ABCs of Probes, Tektronix, Inc., 2018. [Online]. Available: https://www.tek.com/en/documents/whitepaper/abcs-probes-primer

[23] Y. Shi, Z. Xin, P. C. Loh, and F. Blaabjerg, "A review of traditional helical to recent miniaturized printed circuit board Rogowski coils for power-electronic applications," *IEEE Trans. Power Electron.*, vol. 35, no. 11, pp. 12207–12222, Nov. 2020.

[24] J. Wang, S. Mocevic, R. Burgos, and D. Boroyevich, "High-scalability enhanced gate drivers for SiC MOSFET modules with transient immunity beyond 100 V/ns," *IEEE Trans. Power Electron.*, vol. 35, no. 10, pp. 10180–10199, Oct. 2020.

[25] J. Wang, Z. Shen, R. Burgos, and D. Boroyevich, "Design of a high-bandwidth Rogowski current sensor for gate-drive short-circuit protection of 1.7 kV SiC MOSFET power modules," in *Proc. IEEE 3rd Workshop Wide Bandgap Power Devices Appl.*, 2015, pp. 104–107.

[26] J. Wang, Z. Shen, R. Burgos, and D. Boroyevich, "Integrated switch current sensor for short-circuit protection and current control of 1.7-kV SiC MOSFET modules," in *Proc. IEEE Energy Convers. Congr. Expo.*, 2016, pp. 1–7.

[27] J. Wang, S. Mocevic, Y. Xu, C. DiMarino, R. Burgos, and D. Boroyevich, "A high-speed gate driver with PCB-embedded Rogowski switch-current sensor for a 10 kV, 240 A, SiC MOSFET module," in *Proc. IEEE Energy Convers. Congr. Expo.*, 2018, pp. 5489–5494.

[28] S. Mocevic et al., "Phase current sensor and short-circuit detection based on Rogowski coils integrated on gate driver for 1.2 kV SiC MOSFET half-bridge module," in *Proc. IEEE Energy Convers. Congr. Expo.*, 2018, pp. 393–400.

[29] S. M. Kim, R. Burgos, and T. Kwon, "Design of Rogowski switch-current sensor with offset compensation for three-phase SiC inverter," *IEEE Trans. Power Electron.*, vol. 37, no. 10, pp. 11636–11649, Oct. 2022.

[30] Q. Xu et al., "Design of PCB Rogowski coil current sensor with low droop distortion," *IEEE Trans. Power Electron.*, vol. 38, no. 4, pp. 5513–5523, Apr. 2023.

[31] Y. Xue, J. Lu, Z. Wang, L. M. Tolbert, B. J. Blalock, and F. Wang, "A compact planar Rogowski coil current sensor for active current balancing of parallel-connected silicon carbide MOSFETs," in *Proc. IEEE Energy Convers. Congr. Expo.*, 2014, pp. 4685–4690.

[32] X. Zhao et al., "Design of Rogowski coil current sensor integrated with busbar and gate driver for 211 kW SiC-based three-level T-type inverter," in *Proc. IEEE Energy Convers. Congr. Expo.*, 2022, pp. 1–7.

[33] X. Zhao et al., "Design of ultracompact gate driver integrated with current sensor and commutation path for a 211-kW three-level SiC aircraft propulsion inverter," *IEEE Trans. Emerg. Sel. Power Electron.*, vol. 11, no. 4, pp. 4077–4094, Aug. 2023.

[34] J. N. Fritz, C. Neeb, and R. W. De Doncker, "A PCB integrated differential Rogowski coil for non-intrusive current measurement featuring high bandwidth and dv/dt immunity," in *Proc. Power Energy Student Summit*, Jan. 2015, pp. 1–6.
[35] L. Ming, Z. Xin, L. Wei, and P. C. Loh, "Structure and modelling of four-layer screen-returned PCB Rogowski coil with very few turns for high-bandwidth SiC current measurement," *IET Power Electron.*, vol. 13, pp. 765–775, 2020.
[36] S. B. Sohid et al., "PCB Rogowski coil with DC sensing for double pulse test applications," *IEEE Trans. Power Electron.*, vol. 39, no. 4, pp. 4494–4502, Apr. 2024.
[37] K. Wang, X. Yang, H. Li, L. Wang, and P. Jain, "A high bandwidth integrated current measurement for detecting switching current of fast GaN devices," *IEEE Trans. Power Electron.*, vol. 33, no. 7, pp. 6199–6210, Jul. 2018.
[38] J. Wang et al., "Infinity sensor: Temperature sensing in GaN power devices using peak di/dt," in *Proc. IEEE Energy Convers. Congr. Expo.*, 2018, pp. 884–890.
[39] P. S. Niklaus, D. Bortis, and J. W. Kolar, "Beyond 50 MHz bandwidth extension of commercial DC-current measurement sensors with ultra-compact PCB-integrated pickup coils," *IEEE Trans. Ind. Appl.*, vol. 58, no. 4, pp. 5026–5041, Jul./Aug. 2022.
[40] S. Peng and Z. Chen, "High temperature current sensor for power electronics," U.S. Patent 11 740 264, Feb. 5, 2021.
[41] P. Sun, X. Cui, S. Huang, P. Lai, Z. Zhao, and Z. Chen, "LTCC based current sensor for silicon carbide power module integration," *IEEE Trans. Power Electron.*, vol. 37, no. 2, pp. 1605–1614, Feb. 2022.
[42] E. Hoene, A. Ostmann, B. T. Lai, C. Marczok, A. Müsing, and J. W. Kolar, "Ultra-low-inductance power module for fast switching semiconductors," in *Proc. Europe: Int. Exhib. Conf. Power Electron., Intell. Motion, Renewable Energy Energy Manage.*, May 2013, pp. 198–205.
[43] Ingenieurb¨uro Kirill Klein, Rogowski IZM current sensor data sheet, 2019. [Online]. Available: http://ipmdesign.de/currentsensor/CurrentSensorDatasheetAndAppNoteRev1.8.pdf
[44] S. Alexander, "Exploiting the full potential of silicon carbide devices via optimized highly integrated power modules," Doctoral dissertation, RWTH Aachen Univ., Aachen, Germany, 2021.
[45] A. Seshadri, "NSGA - II: A multi-objective optimization algorithm," MATLAB Central File Exchange, 2024, Retrieved: Jun. 18, 2024. [Online]. Available: https://www.mathworks.com/matlabcentral/fileexchange/10429-nsga-ii-a-multi-objective-optimization-algorithm
[46] K. Deb, A. Pratap, S. Agarwal, and T. Meyarivan, "A fast and elitist multiobjective genetic algorithm: NSGA-II," *Trans. Evol. Comp.*, vol. 6, no. 2, pp. 182–197, Apr. 2002.
[47] S. Mocevic, J. Wang, R. Burgos, and D. Boroyevich, "Rogowski switch-current sensor self-calibration on enhanced gate driver for 10 kV SiC MOSFETs," in *Proc. IEEE 12th Energy Convers. Congr. Expo.—Asia*, 2021, pp. 1420–1425.
[48] Z. Zhou, Z. Xin, Q. Liu, and C. Li, "A differential compensated air coil current sensor for switching current measurement of power devices," *IEEE Trans. Ind. Electron.*, vol. 70, no. 5, pp. 5356–5364, May 2023.

Xia Du (Student Member, IEEE) received the B.Eng. degree in automation from Hunan University of Science and Technology, Hunan, China, in 2017, the M.S. degree in electrical engineering from Minnesota State University, Mankato, MN, USA, in 2020, and the Ph.D. degree in electrical engineering from Power MSCAD Group, University of Arkansas, Fayetteville, AR, USA, in 2024.

From 2017 to 2018, she was a General Manager Assistant with Dongguan CHAM Battery Technology Company Ltd., Dongguan, China. She has been working as a Senior Electrical Engineer with Murata Power Solutions, Westborough, MA, USA, since 2024. Her research interests include high bandwidth current sensor design for switching current measurement, active gate driver design, wide bandgap devices, renewable energy integration, and smart grid.

Liyang Du (Student Member, IEEE) received the B.Sc. degree in automation from Shandong University, Jinan, China, in 2017, and the M.Sc. degree in electrical engineering from Tianjin University, Tianjin, China, in 2020. He is currently working toward the Ph.D. degree in electrical engineering with the University of Arkansas, Fayetteville, AR, USA.

In 2020, he worked as an Analog Engineer with Texas Instruments, Shanghai, China. His current research interests include active gate drivers, SiC MOSFET applications, and multilevel converters.

Yuxiang Chen (Member, IEEE) received the B.Sc. degree in electrical engineering and automation and M.Sc. degree in power electronics and power drives from the Department of Information and Electrical Engineering, China University of Mining and Technology, Xuzhou, China, in 2011 and 2014, respectively, and the Ph.D. degree in electrical engineering from the College of Electrical Engineering, Zhejiang University, Hangzhou, China, in 2019.

From 2019 to 2024, she was a Postdoctoral Fellow with the Department of Electrical Engineering and Computer Science, University of Arkansas, Fayetteville, AR, USA, where she is currently serving as an Research Assistant Professor. Her research interests include power device modeling, as well as the design and fabrication of power module packaging.

Andrea Stratta received the B.Eng. degree in energy engineering and the M.Eng. degree in electrical engineering from the University of Pisa, Pisa, Italy, in 2014 and 2017, respectively, and the Ph.D. degree in electrical engineering from the Power Electronics, Machines and Control Group, University of Nottingham, Nottingham, U.K., in 2021.

He was with the German Corporate Research Center of ABB AG, Ladenburg, Germany, in 2017. From 2021 to 2022, he served as a Visiting Research Scholar with the Department of Electrical Engineering and Computer Science, University of Arkansas, Fayetteville, AR, USA, working on optimization of current sensors and active gate driving solutions. He is currently a Research Scholar with the Power Electronics Laboratory, University of California, Irvine, Irvine, CA, USA. His research interests include soft magnetic materials, electromagnetic components integration, and high-power density energy conversion techniques.

Homer Alan Mantooth (Fellow, IEEE) received the B.S. and M.S. degrees in electrical engineering from the University of Arkansas, Fayetteville, AR, USA, in 1985 and 1986, respectively, and the Ph.D. degree in electrical engineering from the Georgia Institute of Technology, Atlanta, GA, USA, in 1990.

He then joined Analogy, a startup company in Oregon, where he focused on semiconductor device modeling and the research and development of modeling tools and techniques. In 1998, he joined the faculty of the Department of Electrical Engineering, University of Arkansas, Fayetteville, AR, USA, where he currently holds the rank of Distinguished Professor. He helped establish the National Center for Reliable Electric Power Transmission (NCREPT) in 2005. He serves as the Executive Director with NCREPT as well as two of its centers of excellence: the NSF Industry/University Cooperative Research Center on GRid-connected Advanced Power Electronic Systems and the Cybersecurity Center on Secure, Evolvable Energy Delivery Systems funded by the U.S. Department of Energy. In 2015, he helped to establish the UA's first NSF Engineering Research Center entitled Power Optimization for Electro-Thermal Systems that focuses on high-power-density systems for transportation applications. His research interests include analog and mixed-signal IC design & CAD, semiconductor device modeling, power electronics, and power electronic packaging.

Dr. Mantooth holds the 21st Century Research Leadership Chair in Engineering. He also serves as Immediate Past-President for the IEEE Power Electronics Society in 2019–2020 and the Editor-in-Chief of IEEE OPEN JOURNAL OF POWER ELECTRONICS. He is a member of Tau Beta Pi and Eta Kappa Nu, and registered Professional Engineer in Arkansas.